Available online at www.sciencedirect.com
SCIENCE DIRECT®
Acta Materialia 53 (2005) 1215–1224
Acta MATERIALIA
www.actamat-journals.com

Near-surface lattice instability in 2D fiber and half-space

S.V. Dmitriev [a,b,*], T. Kitamura [c], J. Li [d], Y. Umeno [c], K. Yashiro [e], N. Yoshikawa [a]

[a] Institute of Industrial Science, University of Tokyo, 153-8505 Tokyo, Japan
[b] National Institute of Materials Science, 1-2-1, Sengen, Tsukuba, Ibaraki 305-0047, Japan
[c] Department of Engineering Physics and Mechanics, Graduate School of Engineering, Kyoto University, Yoshida-hommachi, Sakyo-ku, Kyoto 606-8501, Japan
[d] Department of Materials Science and Engineering, Ohio State University, Columbus, OH 43210, USA
[e] Department of Mechanical Engineering, Faculty of Engineering, Kobe University, 1-1, Rokkodai, Nada-ku, Kobe 657-8501, Japan

Received 17 September 2004; received in revised form 4 November 2004; accepted 6 November 2004
Available online 15 December 2004

Abstract

We study the vibrational stability of model 2D solids with surfaces when large strains are present. For a fiber under compression, the phonon analysis correctly predicts the behavior of the buckling instability. For half-space under tension and compression, we find that (a) instabilities of the surface phonons, which are localized near the surface, almost always occur before bulk phonon instabilities; (b) with exceptions, short-wavelength or optical surface phonons usually go unstable first, rather than long-wavelength acoustic or elastic surface phonons; and (c) linear instability of a surface phonon triggers surface-initiated defect nucleation, such as dislocations or microcracks. The instability pattern seems to depend more on the surface structure than the interatomic potential model used.

Keywords: Surface phonon; Buckling; Dislocation nucleation

1. Introduction

As nanoscale experimental techniques such as atomic force microcopy [1] and instrumented indentation [2] mature, we are beginning to be able to interrogate the inherent strength limits of solids [3]. This is a fundamental development in the mechanics of materials for the following two reasons. The first is that one is interested to know the ultimate strength of an atomic structure, be it crystalline, with defects, or amorphous, when the possibilities of thermally activated processes are excluded. In other words we are interested to know at precisely what stress conditions the saddle energy on some path out of the present potential energy surface basin vanishes. The long wavelength limit of this problem is called elastic instability [4], which can be shown to be mathematically equivalent to spinodal instability [5], but in 6-D strain space instead of composition space. The second important reason is that ideal strength models like the Frenkel formula [6] and universal binding energy relation [7,8] lie at the foundation of continuum theories of defects, such as the Peierls model of dislocation core size [9] and cohesive zone model of crack tip [10]. It can be shown that if only the elastic constant is used, one cannot obtain localized model solution for defect cores; only when the ideal strength is also provided can one regularize the core solution and obtain finite core width. The ideal strengths of a perfect crystal also reflect the nature of electronic bonding in the crystalline bulk [11,12]. For these reasons, it is of interest to compute and compare

* Corresponding author. Tel.: +81 354 526 346; fax: +81 354 526 346.
E-mail address: sergey@iis.u-tokyo.ac.jp (S.V. Dmitriev).

1359-6454/$30.00
doi:10.1016/j.actamat.2004.11.015

the ultimate strength limits of different atomic structures. Many previous work focused on perfect crystals [4,11–15]. In this paper, we study the ultimate strength limits of crystals with a particular kind of defect: surfaces. One expects that such studies will lead eventually to the elucidations of (a) nonlinear surface elasticity [16] and surface-initiated defect nucleation [17], and (b) the electronic bonding state of the surface, parallel to such developments for crystalline bulks.

This problem of the ultimate strength limit (beyond which lattice instability is triggered without thermal activation) has a formally exact solution at $T = 0$ K by normal mode analysis. For any equilibrated atomic structure, one can evaluate and diagonalize the $(3N-6)\times(3N-6)$ force constant matrix (also called the Hessian matrix), where N is the total number of atoms [18,19], and rigid-body translational and rotational motions have been excluded. The eigenvectors thus obtained correspond to the vibrational normal modes, and the eigenvalues correspond to the vibrational frequencies squared. By monitoring all eigenvalues as the external stress is being varied, one can detect when a certain vibrational eigenfrequency turns from real to imaginary, which destabilizes the system [4]. Since the vibrational normal modes form a complete basis for all possible atomic displacements of the system, and since they are energetically decoupled in the $T = 0$ K limit, it is easily seen that the above frequency criterion is both necessary and sufficient to guarantee linear stability of the dynamical system. In perfect crystals, due to translational symmetries, the problem can be further simplified by going to the reciprocal space in all three dimensions. For atomically smooth surfaces, translational symmetry is broken in one dimension, but one can still Fourier transform in the remaining two dimensions, which simplifies the analysis. The long wavelength limit of this problem corresponds to the Rayleigh [20] and Stoneley [21] wave instabilities, and were already studied in the context of elastic–plastic continuum mechanics [22,23]. We now extend this stability analysis to also include short-wavelength, atomic-scale, excitations at $T = 0$ K. For our simple 2D model systems, it will be shown that, under stress, (a) surface phonon instabilities almost always occur before bulk phonon instabilities; (b) with exceptions, short-wavelength or optical surface phonons usually go unstable first, rather than long-wavelength surface (elastic) phonons [24]; and (c) linear instability of a surface phonon triggers surface-initiated defect nucleation, such as dislocations or microcracks [4].

2. Simulation details

An important class of lattice instability is crystals having surfaces or interfaces and no other defects (see, e.g. [19,25]). In this situation the translational symmetry is preserved in one (for a fiber) or two (for a film) directions and the discrete Fourier transform can be effectively applied to reduce the number of degrees of freedom in the stability analysis. In the upper panel of Fig. 1, for the 3D bulk, film and fiber, we show the periodic cells and the translational vectors, **a**, **b**, **c**. For these problems, any small-amplitude displacements of atoms in the vicinity of their equilibrium positions can be presented by a superposition of Fourier harmonics (phonons). For the bulk, film and fiber we have respectively:

$$\mathbf{U}(t) = \mathbf{U}^0 \exp[\mathrm{i}(k_x l + k_y m + k_z n - \omega t)], \tag{1}$$

$$\mathbf{U}(t) = \mathbf{U}^0 \exp[\mathrm{i}(k_x l + k_y m - \omega t)], \tag{2}$$

$$\mathbf{U}(t) = \mathbf{U}^0 \exp[\mathrm{i}(k_x l - \omega t)], \tag{3}$$

where 'i' is imaginary unit; k_x, k_y, k_z are the components of a wavevector in reciprocal space; l, m, n are integer numbers specifying a periodic cell; ω is the eigenfrequency of a particular phonon mode; $\mathbf{U}^0$ is the corresponding eigenvector containing the components of displacements of all atoms in the periodic cell.

When spatial periodicity is absent, such as when we have point defects or kinks on dislocations, local instability can be studied by assuming that the instability mode is localized near the defect. Atoms around the defect are assumed to be movable while the far-

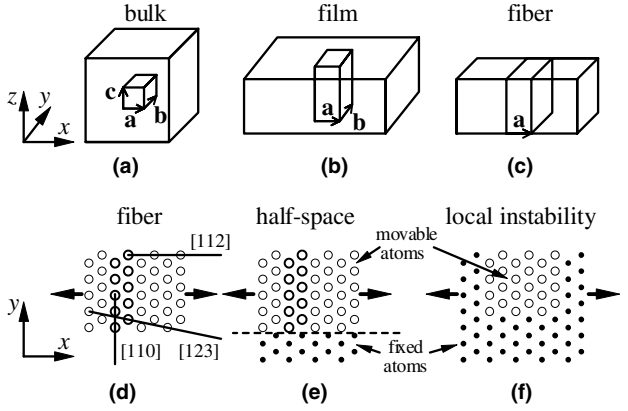

Fig. 1. Upper panel: periodic cells and their translational vectors **a**, **b**, **c** for the 3D instability problems for (a) bulk, (b) film, and (c) fiber. Lower panel: 2D instability problems addressed in the present study, (d) fiber, (e) half-space, (f) embedded-region instability. Instability problems presented in (d) and (e) have translational symmetry in x and are simplified by the discrete Fourier transform. Atoms in a periodic cell are shown by bold open circles. In (e) and (f), movable atoms (open circles) interact with the homogeneously strained continuations of the lattice (dots) which are fixed. Samples are subjected to uniaxial tension or compression along the x-direction, and the surface, which is also parallel to the x-direction, is free of external loads. The case of surface parallel to the [1 1 2] crystallographic orientation (2D triangular lattice is regarded here as a (1 1 1) plane of fcc crystal) is shown in this figure, but we also study the [1 1 0] and [1 2 3] orientations as indicated in (d).

away atoms are fixed at their equilibrium positions. Small-amplitude displacement modes in this case can be expressed as

$$\mathbf{U}(t) = \mathbf{U}^0 \exp(-\mathrm{i}\omega t), \tag{4}$$

where ω is the eigenfrequency of a particular vibrational mode and $\mathbf{U}^0$ is the corresponding eigenvector containing the components of displacements of all movable atoms. This approach is equivalent to that formulated in [19].

Substituting (1)–(4) solution forms into the linearized equations of motion of the atoms gives an eigenvalue problem with $M \times M$ symmetric matrix where M is the number of degrees of freedom in $\mathbf{U}^0$. For the bulk crystal the approach usually can be applied without any complications because the number of atoms in a primitive cell is usually not large. However, for a film or a fiber, the number of degrees of freedom in a periodic cell depends not only on the crystal structure but also on the thickness of the sample and surface orientation. To reduce the number of degrees of freedom one can concentrate on local instabilities [26,27] near the surface. If a structural instability is initiated at the surface, the corresponding instability mode should be localized near the surface, i.e. the displacements of atoms of the unstable eigenmode should decrease rapidly with the distance from the surface. In this situation, in Eqs. (2) and (3), one can set the displacements of atoms far from surface equal to zero thus reducing the number of degrees of freedom in the secular equation. When applying this assumption we exclude the global instabilities from consideration. Special care should be taken when global instability modes can be responsible for the instability of the sample.

In this paper, we study the instability of defect-free 2D crystals having a surface (see the lower panel of Fig. 1). The two-dimensional triangular lattice with lattice parameter a is generated by the vectors $\mathbf{p}_0 = a(1,0)$ and $\mathbf{q}_0 = a(1/2,\sqrt{3}/2)$. In the lattice strained homogeneously with strain components ε_{xx}, ε_{yy}, ε_{xy}, the (i,j)th atom has the position vector $\mathbf{r}_{ij} = i\mathbf{p} + j\mathbf{q}$ where $\mathbf{p} = \mathbf{p}_0 + \mathbf{p}_0\mathbf{H}$, $\mathbf{q} = \mathbf{q}_0 + \mathbf{q}_0\mathbf{H}$, and the matrix $\mathbf{H}$ has coefficients $h_{11} = \varepsilon_{xx}$, $h_{12} = h_{21} = \varepsilon_{xy}/2$, $h_{22} = \varepsilon_{yy}$.

Two different pair interatomic potentials, short-ranged and long-ranged, are employed in this model study. The first is the interatomic potential similar to that used in Van Vliet et al. [28] to simulate the bubble raft indentation:

$$\varphi(r) = \begin{cases} \left(\frac{r-R_c}{R_a-R_c}\right)^8 - 2\left(\frac{r-R_c}{R_a-R_c}\right)^4, & r < R_c, \\ 0, & r \geqslant R_c, \end{cases} \tag{5}$$

where r is the distance between two atoms, R_a is the atom radius and R_c is the cut-off radius. Without the loss in generality we set $R_a = 1$. We set $R_c = 1.3R_a$, i.e. each atom interacts only with the nearest neighbors and thus, lattice parameter is $a = R_a = 1$. The energy unit is chosen in a way that $\varphi(R_a) = -1$. Cohesive energy of the unstrained crystal is equal to $E_0 = -3$ per atom.

The second is the Lennard-Jones potential,

$$\varphi(r) = 4\varepsilon\left[\left(\frac{\sigma}{r}\right)^{12} - \left(\frac{\sigma}{r}\right)^{6}\right], \tag{6}$$

where we set, without the loss in generality, $\varepsilon = 1/4$ and $\sigma = 1$. For the cut-off radius equal to 11, the equilibrium lattice parameter is $a = 1.11146206$. Potential energy per one atom in the unstrained crystal is $E_0 = -0.845459$.

The atomic mass is normalized to unity which can always be done by proper choice of the time unit. Most of the numerical results presented in this paper are obtained with the use of the short-range interatomic potential (5). The long-range Lennard-Jones potential (6) is used in a few cases for comparison. We study the lattice instabilities in 2D fiber and half-space during uniaxial strain (tension or compression) in the direction parallel to the surface (see Fig. 1). The fiber is subjected to periodic boundary condition in axial direction. Half-space is simulated by a rectangular block of atoms with one free surface, one surface interacting with the rigid continuation of the homogeneously strained lattice, and periodic boundary condition along the strain direction. We also study the local near-surface instabilities of an embedded region of a rectangular block of atoms having one free surface and interacting with the rigid continuation of the homogeneously strained lattice on all three other sides (Fig. 1(f)). There is no translational symmetry in this case.

Three simulation substeps are carried out. (i) Pre-critical relaxation of atoms in *one periodic cell* of the sample is simulated under stepwise increase of uniaxial strain. (ii) At each strain step, after the relaxation is complete, we solve the eigenvalue problem to determine the eigenfrequencies ω and eigenmodes $\mathbf{U}^0$ of small-amplitude vibrations of atoms near their equilibrium positions. The eigenvalue problem is formulated by substituting (3) or (4) into the equations of motion of atoms linearized in the vicinity of their equilibrium positions. The number of eigenmodes is equal to the number of degrees of freedom in the (periodic) cell. Vanishing of the frequency of a mode or modes is the criterion of lattice instability. This is the soft phonon mode criterion which is convenient to call the *P*-criterion with the mnemonic *P* standing for "phonon". (iii) Post-critical dynamics of atoms in a supercell consisting of many periodic cells. This simulation is carried out at a fixed external strain slightly exceeding the critical value. Random perturbations of the order of 10^{-3} are introduced in the positions of atoms to excite the fall from the unstable equilibrium.

3. Lattice instabilities in fiber and half-space

To examine the role of surfaces in the lattice instability problem we consider 2D fiber and half-space under uniaxial compression and tension parallel to the surface. Surfaces parallel to the [1 1 0], [1 1 2], and [1 2 3] crystallographic directions (2D triangular lattice is considered here as a (1 1 1) plane of fcc crystal) are studied. Changing the crystallographic orientation of the sample, we change the orientation of the slip systems with respect to the loading axis (Schmid factor), and the atomic structure of the surface as well.

3.1. Vibrational spectra of compressed fiber and half-space

The difference in lattice instabilities of fiber and half-space can be seen by comparing their phonon dispersion curves. In Fig. 2 we show the dispersion curves for (a) fiber and (b) half-space compressed along the direction parallel to the surface having [1 1 2] orientation with the nearly critical magnitude of strain, $\varepsilon_{[1\,1\,2]} = -0.0524$. A periodic cell of fiber (half-space) contains 40 (20) atoms, i.e. 80 (40) degrees of freedom. The number of branches of the dispersion curves is equal to the number of degrees of freedom. Lower panels show the low-frequency parts of the spectra. The half-space problem has no translational invariance because the movable atoms interact with fixed atoms. Consequently, all modes in the half-space are the optical modes. Fiber has two acoustic modes both containing transverse and longitudinal components (mixed TA and LA modes).

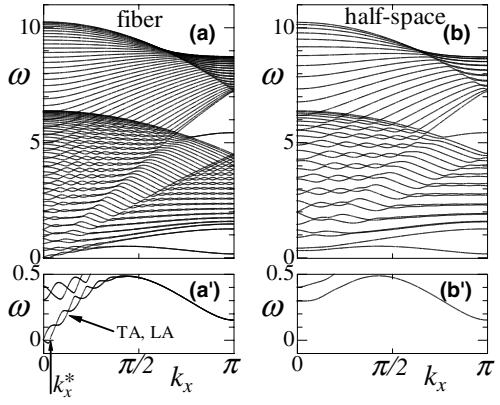

Fig. 2. Comparison of the phonon dispersion curves for (a) fiber and (b) half-space compressed along the direction parallel to the surface having [1 1 2] orientation with the strain $\varepsilon_{[1\,1\,2]} = -0.0524$, which is slightly smaller than critical magnitude, $\varepsilon^*_{[1\,1\,2]} = -0.05245$, when the lowest mode turns unstable at the zone boundary, $k_x = \pi$. A periodic cell of fiber (half-space) contains 40 (20) atoms and thus, 80 (40) degrees of freedom. The number of branches of the dispersion curves is equal to the number of degrees of freedom. Lower panels show the low-frequency parts of the spectra. Fiber under compression is always unstable against long-wavelength global buckling mode as seen in (a′) (for $\omega^2 < 0$ we plot $-\sqrt{-\omega^2}$). The maximum wave-vector with imaginary frequency is labeled as k_x^*.

Spectra of fiber and half-space retain some features of the spectrum of the infinite 2D triangular lattice. Periodic cells in fiber and in half-space with surfaces having [1 1 2] orientation contain two monatomic layers in x-direction and many layers in y-direction (see Fig. 1 (d) and (e)) that is why, in Fig. 2, one can distinguish double-folded and multiple-folded dispersion curves. For fiber, the dispersion curves are winded by two (compare Fig. 2(a′) and (b′)). This is because a fiber has two surfaces and every eigenmode has nearly axisymmetric counterpart with nearly the same frequency.

Both for fiber and half-space, the lowest phonon branch softens appreciably at the zone boundary, $k_x = \pi$, at $\varepsilon^*_{[1\,1\,2]} = -0.05245$. However, in the fiber, as is seen in (a′), the imaginary frequencies near the origin of the first Brillouin zone, $k_x = 0$, are observed at $\varepsilon_{[1\,1\,2]} < \varepsilon^*_{[1\,1\,2]}$ (for $\omega^2 < 0$ we plot $-\sqrt{-\omega^2}$). This instability with respect to long-wave modes is simply the global buckling mode of the fiber under compressional load.

To confirm the last statement we denote the maximum wave-vector with imaginary frequency as k_x^* (see Fig. 2(a′)) and check how the critical length of fiber, $L^* \sim 1/k_x^*$, depends on the fiber thickness, h. According to the classical Euler's formula for column buckling, critical axial stress is $\sigma^* \sim EI/(SL^2)$, where E is the elastic modulus, L is the length of the column, $S = bh$ and $I = bh^3/12$ are the area and the moment of inertia of the column cross-section having width b and thickness h. One can fix the axial stress σ^* near the bulk ideal strength and consider the critical length L^* as the function of thickness h and obtain $L^* \sim h$. Our numerical results are in excellent agreement with the Euler's formula prediction for a wide range of fiber thickness h measured in units of lattice parameter a. We found that $L^* \sim 1/k_x^* = 0.53(h/a) - 1.7$. The relation $L^* \sim h$ means that the region with imaginary frequencies near $k_x = 0$ never disappears from the spectrum of fiber under compression. If the periodic cell used in MD simulation is shorter than L^*, fiber is stable because there is not enough length to establish the unstable mode in the periodic cell. Note that the Euler's formula gives the correct qualitative result but it may not give a correct magnitude of the coefficient. It is insufficient just to use this formula with the current elastic modulus E in the case when the critical stress is comparable to E (see, e.g. [29]).

3.2. Instabilities in fiber

Here, we do not aim to analyze the instability of very thin fibers consisting of just a few monolayers but we are interested in critical strains and instability modes of rather thick fibers for which the thickness is already not important. In Fig. 3 we show the low-frequency part

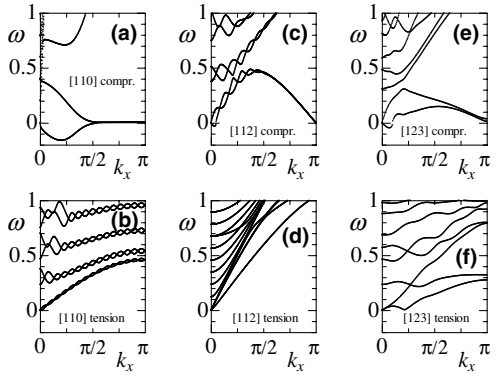

Fig. 3. Instabilities in fiber. Low-frequency part of the spectra of fibers is shown at respective critical values of strain. The results are for compression (upper panels) and tension (lower panels) for fibers having surface orientations (a,b) [1 1 0]; (c,d) [1 1 2]; and (e,f) [1 2 3]. Corresponding critical values of strain are presented in Fig. 5 as the functions of fiber thickness.

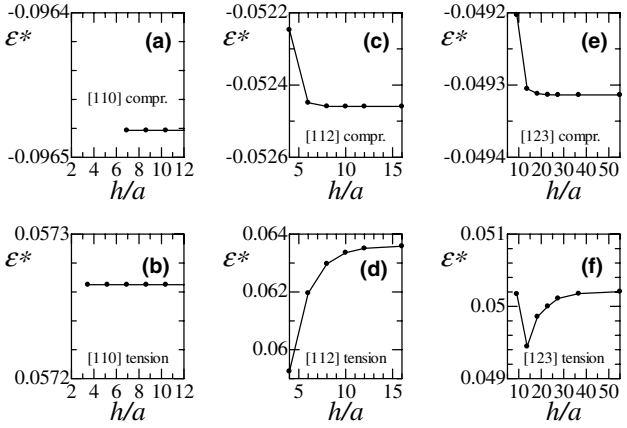

Fig. 5. Critical strain, ε^*, as the function of fiber thickness, h, measured in units of lattice parameter a. The results are for compression (upper panels) and tension (lower panels) for fibers having surface orientations (a,b) [1 1 0]; (c,d) [1 1 2]; and (e,f) [1 2 3].

of the spectra of fibers under compression (upper panels) and tension (lower panels) at the critical strain parameter, when a particular branch of the spectrum vanishes. Three different surface orientations, [1 1 0], [1 1 2], and [1 2 3], are studied. The corresponding unstable eigenmode displacements are illustrated in Fig. 4. Critical values of strain are given in Fig. 5 as the functions of fiber thickness.

As discussed above and shown in the upper panels of Fig. 3, fiber under compression always contains imaginary frequencies near $k_x = 0$ corresponding to the global buckling mode. The domain of k_x with imaginary frequencies decreases with increase in fiber thickness. But now we will show the short-wavelength instabilities not related to buckling, which are important for rather

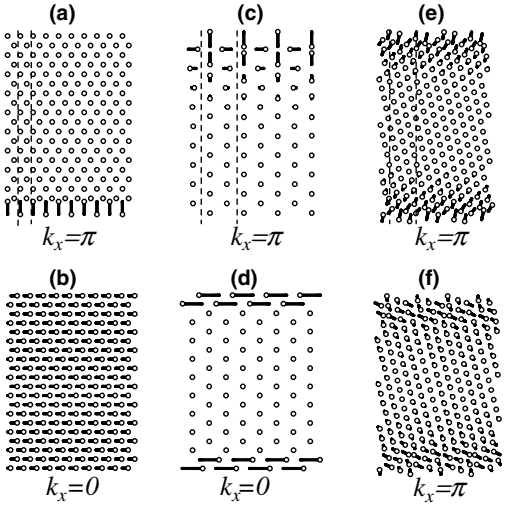

Fig. 4. (a)–(f) Eigenmode displacements corresponding to the instabilities of fiber shown in Fig. 3(a)–(f), respectively. Unstable mode in (b) is not localized at the surface while all the other modes are surface local modes and the displacement amplitudes of atoms reduce exponentially with the distance from the surface. Vertical dashed lines in upper figures show a periodic cell.

thick and short fibers. In Fig. 3(a), the stress is chosen such that instability takes place simultaneously for all short-waves, while in (c) and (e) only for the $k_x = \pi$ modes. Unstable modes presented in Fig. 4(c) and (e) are the surface instability modes where the amplitudes of atomic displacement decrease exponentially with depth. The unstable mode shown in Fig. 4(a) is even more extreme in that it is sharply localized in just one atomic monolayer. We note that the modes presented in Fig. 4(a) and (c) are localized at one surface of fiber but they have symmetric counterparts having practically the same near-zero frequency and localized at the other surface.

[1 1 0] fiber under tension is the only case when, despite the presence of surface, which can be regarded as a crystal defect, the instability mode is the elastic mode corresponding to vanishing of sound velocity, see Figs. 3(b) and 4(b). Tensions along [1 1 2] and [1 2 3] result in near-surface local instabilities. However, tension along [1 1 2] is unstable with respect to an optical mode at $k_x = 0$ and this mode is sharply localized in two monatomic layers (see (d) in Figs. 3 and 4). Tension along [1 2 3] is unstable with respect to an exponentially localized mode (see Fig. 4(f)). It should be noted that vanishing of the dispersion curve in Fig. 3(f) occurs not at $k_x = \pi$ but inside the first Brillouin zone, closer to $k_x = 0$. However, this result was obtained for rather thin fiber in order to keep approximately the same number of degrees of freedom as in other cases, but for sufficiently thick fiber the mode softens at $k_x = \pi$.

Tension along [1 1 2] is the only case where not acoustic but optical mode softens. This case is also exceptional with respect to the post-critical behavior. In all other cases the instabilities are rather cataclysmic and they result in dislocation nucleation and gliding and, for rather long fiber under tension, in fiber fracture. But in the case of tension along [1 1 2], the instability

with respect to the mode depicted in Fig. 4(d) results in surface reconstruction in two monatomic layers closest to the surface. This is more like second-order phase transition when, at the critical strain, two monolayers deviate from the symmetric position by a small amount equivalently to the right or to the left. As the result of this reconstruction, the unstable mode hardens until a global instability is achieved. For rather long fiber, due to the probabilistic character of surface reconstruction, formation of domains with surface atoms deviated to the right or to the left can take place. In this case, the domain walls (kinks) separating domains of different sign would appear and they may influence the forthcoming global instability. However, we do not pursue this interesting problem here.

3.3. Influence of interatomic potential

In Fig. 6 we present the same results as in Fig. 3 but for the Lennard-Jones interatomic potential (6) instead of potential (5). One can see that the change from the short-range to the long-range potential results only in quantitative but not in qualitative changes in spectra and in the instability mechanisms. Magnitudes of critical strains for (a) and (b) are $\varepsilon^* = -0.09754$ and $\varepsilon^* = 0.11970$; for (c) and (d) are $\varepsilon^* = -0.07579$ and $\varepsilon^* = 0.13037$; for (e) and (f) are $\varepsilon^* = -0.06612$ and $\varepsilon^* = 0.10633$, respectively. The absolute values of these magnitudes are larger than in the case of the short-range potential (see in Fig. 5). This is consistent with the fact that for the crystalline bulk instabilities the critical strains are also larger for the long-range instabilities [30]. The instability modes obtained for fiber with the Lennard-Jones potential are also similar to that presented in Fig. 4 for the short-range potential.

Thus we did not find any essential difference between results obtained with the use of short- and long-range interatomic potentials (compare Figs. 3 and 6). However, fibers having different orientations exhibit very different instability behavior in terms of dispersion curve vanishing points and instability displacements. We come to the conclusion that in our numerical setup the atomic structure of the surface and the crystallographic orientation of the fiber play more important role in controlling the instability mechanism than the actual law of interatomic interactions.

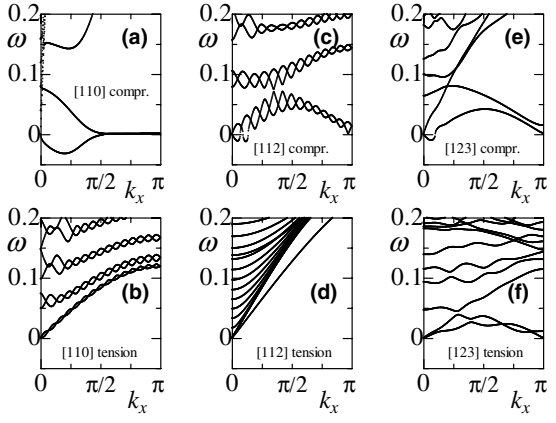

Fig. 6. Same as in Fig. 3 but here, for the sake of comparison, we used the long-range Lennard-Jones potential (6) instead of short-range potential (5).

3.4. Surface local instabilities in half-space

Analyses of instabilities in fibers have shown that, except for the tension of [1 1 0] fiber having atomically flat surface, the instability modes in all other cases are localized near surface. For such modes one can considerably reduce the number of degrees of freedom noting that the amplitude of vibration of atoms situated far from the surface is negligibly small. Thus we come to the half-space instability problem schematically depicted in Fig. 1(e).

In Fig. 7 we show the low-frequency part of spectra of the half-spaces under compression (upper panels) and tension (lower panels) at the critical strain parameter, for the three different orientations. Corresponding unstable eigenmode displacements are depicted in Fig. 8 and the corresponding MD results showing the initial stages of the post-critical transformations are presented in Fig. 9. The results for half-space, Figs. 7 and 8, should be compared to the results for fiber, Figs. 3 and 4, respectively.

Recall that, in contrast to the fiber instability problem, in the half-space problem the vibrational spectra do not have acoustic branches. Global buckling instability is not possible for half-space and for this reason, in the upper panels of Fig. 7 we do not have imaginary frequencies near $k_x = 0$, as it was observed in corresponding panels of Fig. 3 for fiber. Otherwise the spectra of fiber and half-space resemble each other. Similar to what was observed for fiber, only tension along [1 1 2], panel

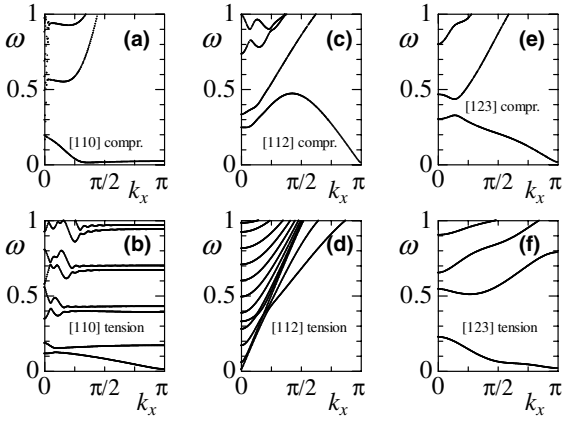

Fig. 7. Low-frequency part of the spectra of half-spaces at critical values of strain. The results are for compression (upper panels) and tension (lower panels) in the direction parallel to the surface for the surface orientations (a,b) [1 1 0], (c,d) [1 1 2], and (e,f) [1 2 3].

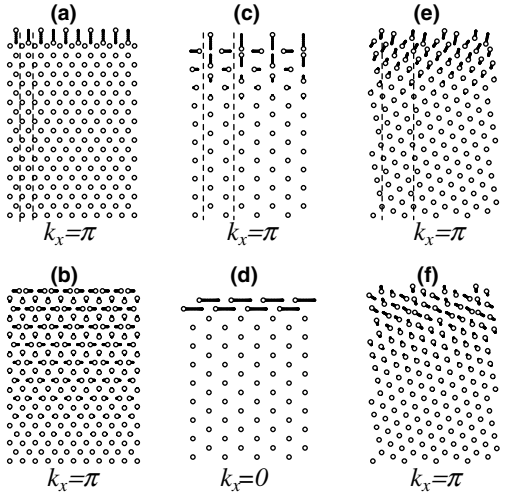

Fig. 8. (a)–(f) Soft eigenmodes corresponding to the instabilities shown in Fig. 7(a)–(f), respectively. Unstable mode in (b) is not localized at the surface (decrease of the displacement amplitude away from the surface is linear but not exponential) while the other modes are the surface modes and the displacements of atoms reduce very rapidly with the distance from the surface. Only movable atoms are shown. Vertical dashed lines in upper figures show a periodic cell.

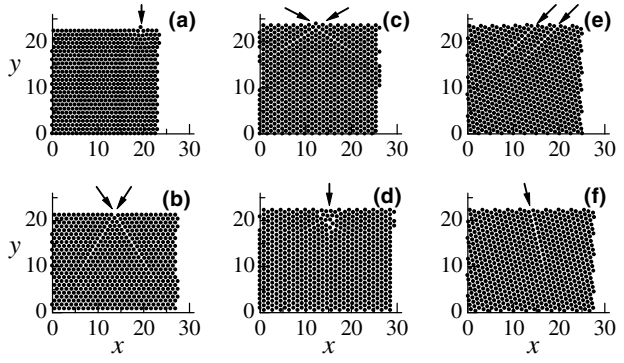

Fig. 9. Initial stage of the post-critical structural transformations simulated by MD. Panels (a)–(f) correspond to the results presented in Figs. 7(a)–(f) and 8(a)–(f), respectively. In (a), the transformation starts in the single surface monolayer, in (d) it starts from surface reconstruction which affects only two monolayers (cannot be seen here) followed by spinodal decohesion (micro-cracking), and in all other cases the transformation starts from the generation of dislocations at the surface and their gliding in the main slip system.

(d), results in the mode softening at the origin of the Brillouin zone, $k_x = 0$, while in all other cases mode softening occurs either at the zone boundary, $k_x = \pi$, or inside the first Brillouin zone, as in (a).

Unstable displacement modes of fiber (Fig. 4) and half-space (Fig. 8) are also alike except for the case of tension along [1 1 0] presented in (b). The difference in this case is due to the fact that the half-space problem does not permit the global instability mode (vanishing of sound velocity) which is responsible for the instability in fiber.

Critical values of strain for half-space with increase in thickness of movable atom region approach corresponding values for rather thick fiber (see Fig. 5) except for the case in (b). Here, we have $\varepsilon^* = 0.0583$ for half-space and $\varepsilon^* = 0.0573$ for fiber.

MD simulations of the post-critical behavior confirmed the dislocation mechanism of the structural transformations in all cases studied here. However, the dislocations do not appear at the very initial stage of the structural transformations in the cases presented in Fig. 3(a) and (d). In Fig. 3(a), in accordance with the highly-localized structure of the soft eigenmode presented in Fig. 4(a), the transformation starts in the single surface monolayer. In Fig. 3(d), transformation starts from micro-cracking near the surface. In all other cases one can observe the generation of dislocations at the surface and their gliding in the main slip system.

3.5. Comparison to the bulk instability

In Fig. 10 we compare the results of instability in the bulk with the instabilities in fiber and half-space having [1 1 0] and [1 1 2] crystallographic orientations (shown in the inset). Compression/tension along these directions does not cause the appearance of shear strain and the strain state of fiber or half-space can be presented in the plane ($\varepsilon_{[1\,1\,0]}$, $\varepsilon_{[1\,1\,2]}$). Surface of fiber and half-space is free of external load, i.e. stress perpendicular to the direction of strain is equal to zero. Thin dash-dotted lines 1 and 2 are the trajectories of uniaxial stress of bulk crystal with zero stress in perpendicular direction. One can see that in a wide range of strain along [1 1 0], Poisson's ratio is practically constant and equals to the small-strain value 1/3. To the contrast, in straining along [1 1 2], Poisson's ratio deviates significantly from 1/3

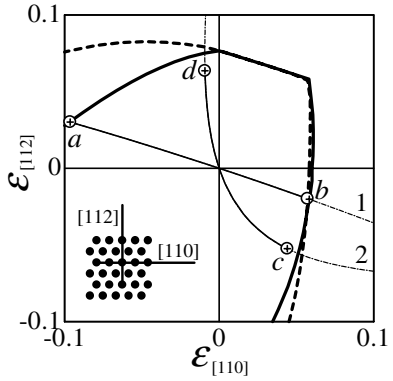

Fig. 10. Comparison of the results of instability in the bulk with the instabilities in fiber and half-space having surface orientations [1 1 0] and [1 1 2] (shown in the inset). Thin dash-dotted lines 1 and 2 are the trajectories of uniaxial stress of bulk crystal with zero stress in perpendicular direction. Thick solid line and thick dashed line show the borders of stability regions of the bulk crystal with respect to a soft phonon mode (*P*-criterion) and with respect to a homogeneous strain mode (*B*-criterion), respectively. Trajectories *ab* and *cd* present the stable deformation of fiber and half-space with crystallographic orientations [1 1 0] and [1 1 2], respectively. Critical points *a*, *b*, *c*, *d* are shown for fiber by open circles and for half-space by crosses.

approaching zero in compression and a large positive value in tension.

Thick solid line and dashed line in Fig. 10 show the borders of stability regions of the bulk crystal with respect to a soft phonon mode (*P*-criterion) and with respect to a homogeneous strain mode (*B*-criterion), respectively. The results for bulk instability have been discussed in [30].

Trajectories *ab* and *cd* show the stable deformation of fiber and half-space with crystallographic orientations [1 1 0] and [1 1 2], respectively. One can see that the [1 1 2] surface noticeably affects the critical strain values, while in the case of [1 1 0] orientation the effect of surface on the critical strain values is marginal. The results for the [1 2 3] half-space cannot be presented in the plane ($\varepsilon_{[1\,1\,0]}$, $\varepsilon_{[1\,1\,2]}$) but the reduction of the critical strain compared to the bulk critical value is even more remarkable than for the [1 1 2] surface. This can be easily understood because the [1 1 0] surface is the atomically flat close-packed one while the [1 1 2] and especially the [1 2 3] surface are rough. These results suggest the importance of taking into account the steps on the surfaces.

4. Embedded-region instability

Now we turn to the lattice instability problem in the absence of translational symmetry. This approach can be applied to predict the near-defect local instabilities, e.g. near a kinked step on a surface, near a dislocation in the bulk, near a crack tip, etc. However, here we apply this approach to the analysis of the periodic surface to have a possibility to compare the results with that obtained above. The main idea of using the local instability analysis is to decrease the number of degrees of freedom. Only atoms near the defect are assumed to be movable and they interact with rigid continuation of the strained equilibrium lattice, as it is schematically shown in Fig. 1(f). Surface plays the role of defect in our case.

Let us consider the [1 1 0] surface under tension/compression, because in this case we can compare the situation when the instability mode is localized near the surface, as it is in compression (see Figs. 4(a) and 8(a)), with the situation when the instability mode is not localized, as it is in tension (see Figs. 4(b) and 8(b)).

In Fig. 11 we show the instability modes for (a) compression and (b) tension parallel to surface. Only movable atoms are shown. In this example, the region with movable atoms consists of $N_x = 20$, $N_y = 16$ monolayers.

The mode in Fig. 11(a) should be compared to that depicted in Fig. 4(a) and Fig. 8(a). One can see that this is actually the same mode subjected to clamping boundary conditions, analogous to forming a Gaussian wave pack or wavelet out of plane waves. The similarity of

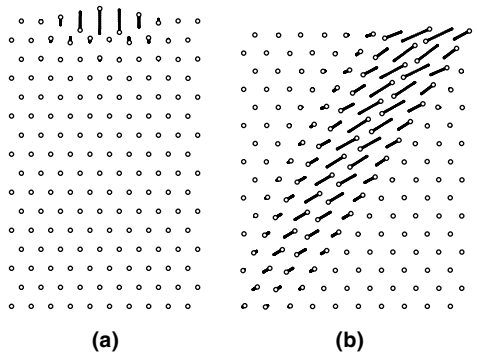

Fig. 11. Instability modes in the embedded-region instability analysis for [1 1 0] surface. Samples in (a) and (b) are under compression and tension parallel to surface, respectively. Only movable atoms are shown. Number of monolayers along x and y directions is equal to $N_x = 20$, $N_y = 16$.

the instability modes ensures good estimation of the critical strain even for the size of the movable region considerably smaller that that presented in Fig. 11(a). Influence of the size of movable region on the critical strain is presented in Fig. 12(a). With increase in N_x, N_y, the result converges very rapidly to the critical strain value obtained for rather thick fiber and half-space (shown by horizontal dashed line).

For the non-local instability mode observed in tension the situation is not as good as for localized mode observed in compression. Indeed, the soft mode obtained in local instability analysis and presented in Fig. 11(b) differs from the homogeneous acoustic mode observed in fiber and depicted in Fig. 4(b) but it resembles the staggered instability mode in Fig. 8(b), observed for half-space. Recall that we got somewhat smaller critical strain for fiber compared to that for half-space because in the latter case the acoustic phonon branch, which is responsible for the instability of fiber, is absent. The critical strains for fiber and half-space are shown in Fig. 12(b) by dashed horizontal lines 1 and 2, respectively. With increase in N_x, N_y, the result of local lattice

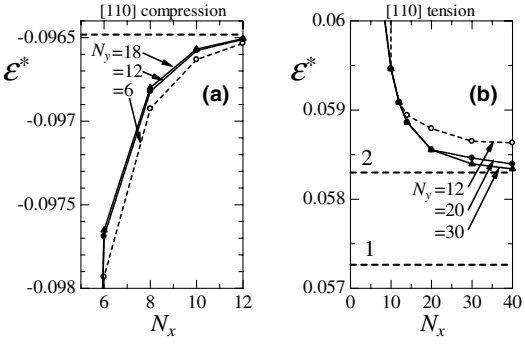

Fig. 12. Critical strain for the embedded-region instability analysis for different size of the region with movable atoms, measured in number of monolayers along x and y directions, N_x, N_y. Dashed horizontal line in (a) shows the critical value obtained for rather thick fiber and half-space. Dashed horizontal lines 1 and 2 in (b) show the critical values obtained for rather thick fiber and half-space, respectively.

instability analysis converges to the critical strain value obtained for half-space but not to that for fiber.

Thus, the results of local lattice instability analysis are in agreement with our expectation. This method allows one to obtain a very good approximation for a localized instability modes but it does not show convergence when the instability mode is a homogeneous strain mode.

5. Conclusions and discussions

The role of surface in the lattice instability problem has been studied numerically for 2D crystal model. To clarify the local vs. global instability issue, first we studied the instability of 2D fiber and then compared the results with the calculations for 2D half-space taking into account only the near-surface instability modes. Substitution of rather thick fiber with a half-space may result in considerable reduction of the number of degrees of freedom without the loss in the accuracy for the instability modes localized near surface. Instability analysis for defect-free fiber or half-space can be conveniently done in terms of Fourier-harmonics using the spatial periodicity of the problem. As an alternative approach, we also applied the method developed in [19]. Their method has been developed for the local instability analysis in the absence of spatial periodicity but we have found that, with increase in the number of degrees of freedom, it shows rather fast convergence for the defect-free fiber and half-space too.

The influence of surfaces orientation has been studied. We always applied homogeneous tension/compression parallel to surface and thus, changing the crystallographic orientation of the sample, we changed not only the structure of the surface but also the orientation of the slip systems with respect to the loading axis (Schmidt factor). Particularly we have studied surfaces having [1 1 0], [1 1 2], and [1 2 3] crystallographic orientations (2D triangular lattice is considered here as a (1 1 1) plane of fcc crystal) with [1 1 0] surface being atomically flat, [1 1 2] surface being rough, and [1 2 3] surface being quasi-vicinal. Only in the case of tension of [1 1 0] fiber the instability with respect to homogeneous strain mode was responsible for the collapse of the system while in all other cases a local near-surface instability preceded global one. Among these cases, only in tension of [1 1 2] fiber, local instability was not the catastrophic one and it resulted in a local near-surface atomic reconstruction followed soon by a catastrophic global instability. In all other cases the collapse of the system was observed due to a near-surface local instability mode. Thus, surfaces under compression were always unstable with respect to a local mode and surfaces under tension demonstrated global instabilities for low-index orientations and local instabilities for high-index orientations. This trend also suggests that, in a realistic situation with steps on surface, local instabilities can control the strength of the surface under homogeneous strain.

We have found that the critical strains for near-surface lattice instabilities can be noticeably lower than that in bulk instabilities. Analysis of the post-critical atomic reconstruction by molecular dynamics revealed that it begins as prescribed by the instability mode. We did not find any essential difference between results obtained with the use of short- and long-range interatomic potentials. However, fibers having different orientations exhibit very different instability behavior. We come to the conclusion that in our numerical setup the atomic structure of the surface and the crystallographic orientation of the fiber play more important role in controlling the instability mechanism than the actual law of interatomic interactions.

Here, we used the phonon mode criterion of instability which is a microscopic one. An attempt to construct a phenomenological approach and to derive a phenomenological criterion of lattice instability will be discussed elsewhere. One difficulty we have in constructing a phenomenological theory for the surface or the interface instability is the short-wave character of the unstable mode in combination with the homogeneous strain condition. Thus, the continuum theory should be capable of taking into account the coupling of short and long waves. Such a theory can be constructed with the use of the Vasiliev's multi-field approach [31–33]. Another difficulty is that in some cases the unstable mode is sharply localized at a few near-surface monolayers and a continuum description becomes questionable. On the other hand, there are many examples where the localization is exponential and a continuum approach can be applied. The results for interfacial instabilities of bilayers under coherency and externally applied homogeneous strain will be reported in a forthcoming paper.

Acknowledgements

SVD wishes to thank the Nanostructure Coating Project carried out by New Energy and Industrial Technology Development Organization (NEDO) for their financial support. JL acknowledges support by Honda R&D Co., Ltd. and the OSU Transportation Research Endowment Program.

References

[1] Binnig G, Rohrer H. Rev Mod Phys 1999;71:S324.
[2] Gouldstone A, Koh HJ, Zeng KY, Giannakopoulos AE, Suresh S. Acta Mater 2000;48:2277.
[3] Lorenz D, Zeckzer A, Hilpert U, Grau P, Johansen H, Leipner HS. Phys Rev B 2003;67:172101.
[4] Li J, Ngan AHW, Gumbsch P. Acta Mater 2003;51:5711.

[5] Lupis CHP. Chemical thermodynamics of materials. New York: North-Holland; 1983.
[6] Frenkel J. Z Phys 1926;37:572.
[7] Rose JH, Ferrante J, Smith JR. Phys Rev Lett 1981;47:675.
[8] Rose JH, Smith JR, Ferrante J. Phys Rev B 1983;28:1835.
[9] Peierls R. Proc Phys Soc London 1940;52:34.
[10] Hong SS, Kim KS. J Mech Phys Solids 2003;51:1267.
[11] Ogata S, Li J, Yip S. Science 2002;298:807.
[12] Ogata S, Li J, Hirosaki N, Shibutani Y, Yip S. Phys Rev B 2004;70:104104.
[13] Li J, Van Vliet KJ, Zhu T, Yip S, Suresh S. Nature 2002;418:307.
[14] Zhu T, Li J, Van Vliet KJ, Ogata S, Yip S, Suresh S. J Mech Phys Solids 2004;52:691.
[15] Umeno Y, Kitamura T. Mater Sci Eng B 2002;88:79.
[16] Cammarata RC. Prog Surf Sci 1994;46:1.
[17] Juan YM, Sun YM, Kaxiras E. Phil Mag Lett 1996;73:233.
[18] Kitamura T, Umeno Y, Fushino R. Mater Sci Eng A 2004;379:229.
[19] Kitamura T, Umeno Y, Tsuji N. Comp Mater Sci 2004;29:499.
[20] Rayleigh JWS. The theory of sound. New York: Dover Publications Inc; 1945.
[21] Stoneley R. Proc R Soc London 1924;106:416.
[22] Needleman A, Ortiz M. Int J Solids Struct 1991;28:859.
[23] Suo Z, Ortiz M, Needleman A. J Mech Phys Solids 1992;40:613.
[24] Clatterbuck DM, Krenn CR, Cohen ML, Morris JW. Phys Rev Lett 2003;91:135501.
[25] Yashiro K, Tomita Y. J Phys IV 2001;11:3.
[26] Li J, Yip S. Phys Rev B 1997;56:3524.
[27] Jayanthi CS, Tang M, Wu SY, Cocks JA, Yip S. Phys Rev Lett 1997;79:4601.
[28] VanVliet KJ, Li J, Zhu T, Yip S, Suresh S. Phys Rev B 2003;67:104105.
[29] Bazant ZP. J Appl Mech-T ASME 2003;70:75.
[30] Dmitriev SV, Li J, Yoshikawa N, Shibutani Y. Phil Mag, in press.
[31] Vasiliev AA. Moscow Univ Mech Bull 1996;51:44.
[32] Dmitriev SV, Shigenari T, Vasiliev AA, Abe K. Phys Rev B 1997;55:8155.
[33] Vasiliev AA, Dmitriev SV, Miroshnichenko AE. Int J Solids Struct, in press.